# Experimental and numerical investigation on the role of holes arrangement on the heat transfer in impingement/effusion cooling

https://doi.org/10.1016/j.ijheatmasstransfer.2018.06.102

# Experimental and numerical investigation on the role of holes arrangement on the heat transfer in impingement/effusion cooling schemes

Antonio Andreini[a,*], Lorenzo Cocchi[a], Bruno Facchini[a], Lorenzo Mazzei[a], Alessio Picchi[a]

[a] *Department of Industrial Engineering DIEF, University of Florence, Via di Santa Marta 3, 50139 Florence, Italy*

**Abstract**

In the present work, two different impingement/effusion geometries have been investigated, both having staggered hole configuration and an equal number of impingement and effusion holes. The first geometry, which is designed in case of low coolant availability, has impingement hole pitch-to-diameter ratios of 10.5 in both orthogonal directions, a jet-to-target plate spacing of 6.5 hole diameters, with effusion holes inclined of 20° with respect to the target surface. The second geometry, which is designed in case of high coolant availability, has impingement hole pitch-to-diameter ratios of 3.0, a jet-to-target plate spacing of 2.5 diameters and normal effusion holes. For each geometry, two relative arrangements between the impingement and effusion holes have been investigated, as well as various Reynolds numbers for the sparser geometry. The experimental investigation has been performed by applying a transient technique, using narrow band thermochromic liquid crystals (TLCs) for surface temperature measurement. A CFD analysis has also been performed in order to support interpretation of the results. Results show unique heat transfer patterns for every investigated geometry. Weak jet-jet interactions have been recorded for the sparser array geometry, while intense secondary peaks and a complex heat transfer pattern are observed for the denser one, which is also strongly influenced by the presence and position of effusion holes. For both the geometries, effusion holes increase heat transfer with respect to impingement-only, which can be mainly attributed to a reduction in flow recirculation for the sparser geometry and to the suppression of spent coolant flow for the denser one.

*Keywords:* impingement, effusion, cooling, heat transfer coefficient, liquid crystals, CFD, SAS

## 1. INTRODUCTION

Gas turbine development is characterized by a continuously increasing turbine inlet temperature, which is beneficial for the efficiency and power output of the engine. The main drawback of this trend is the corresponding enhancement of thermal loads on all engine components exposed to the hot gas flow. To sort out this issue, cooling systems have been developed to keep material temperatures to a level that ensures an adequate lifespan of hardware. In modern gas turbines, different cooling techniques are usually applied simultaneously: the interaction among the various systems can strongly affect the performances of

*Corresponding Author
*Email address:* antonio.andreini@unifi.it (Antonio Andreini)

**Nomenclature**

**Acronyms**

| | |
|---|---|
| $CFD$ | Computational Fluid Dynamics |
| $HTC$ | Heat Transfer Coefficient $[W/mK]$ |
| $RANS$ | Reynolds-Averaged Navier-Stokes |
| $SAS$ | Scale Adaptive Simulation |
| $TLC$ | Thermochromic Liquid Crystals |

**Greek symbols**

| | |
|---|---|
| $\alpha$ | thermal diffusivity $[m^2/s]$ |
| $\beta$ | angle respect to plate $[deg]$ |
| $\mu$ | dynamic viscosity $[Pa/s]$ |

**Latin symbols**

| | |
|---|---|
| $\dot{m}$ | mass flow rate $[kg/s]$ |
| $A$ | area $[m^2]$ |
| $D$ | diameter $[m]$ |
| $G$ | mass flow rate over area ratio $[kg/m^2s]$ |
| $h$ | convective heat transfer coefficient $[W/m^2K]$ |
| $k$ | thermal conductivity $[W/mK]$ |
| $N$ | number of holes $[-]$ |
| $Nu$ | Nusselt number $[-]$ |
| $Re$ | Reynolds number $[-]$ |
| $S$ | thickness $[m]$ |
| $T$ | temperature $[K]$ |
| $t$ | time $[s]$ |
| $x$ | streamwise direction $[m]$ |
| $X$ | jet-to-jet spacing ($x$ direction) $[m]$ |
| $y$ | lateral direction $[m]$ |
| $Y$ | jet-to-jet spacing ($y$ direction) $[m]$ |
| $Z$ | jet-to-target plate spacing $[m]$ |

**Subscripts**

| | |
|---|---|
| 0 | Geometry 2 (impingement only), first row |
| $e$ | effusion |
| $i$ | impingement |
| $init$ | initial |
| $j$ | impingement jet |
| $w$ | wall |

the single system. Accordingly, a study of the complete cooling configuration is often required to determine its performance: some interesting applications can be found in previous studies carried out by the authors [1, 2, 3].

A highly effective cooling system, widely used in combustor liners and nozzle guide vanes, is the combination of impingement and effusion cooling. In this configuration an array of impinging jets is generated by a perforated baffle which cools down the wall opposite to the hot gas path. The spent coolant then feeds an array of effusion holes through the target wall itself and is evacuated on the hot side, creating a protective film layer. The area averaged heat transfer coefficient (HTC) on the cold side of the target wall can be up to 55% higher than the ones obtained with impingement alone [4], and up to 10 times the values of effusion only [5]. Heat transfer enhancement by impingement alone is dependent upon the suppression of spent coolant

flow (crossflow), which deflects coolant jets and degrades impingement performance [4, 6, 7]. The interaction between impingement and effusion flow fields can increase heat transfer even without crossflow, mainly thanks to the reduction of flow re-entrainment [8, 9], while a minor role seems to be played by flow acceleration near the effusion holes [8, 10]. The presence of impingement plate itself can also be beneficial for hot gas side protection [11]. The overall pressure drop across the liner is indeed distributed between the two layers with the impingement perforations usually set as metering orifices for prescribing the mass flow. This allows to maintain high effusion holes apertures with a reduced pressure drop thus decreasing the jet penetration and improving film cooling development[12].

According to previous discussion, it is evident that impingement/effusion cooling schemes represent a feasible strategy to increase cooling efficiency and save coolant. However, the implementation of such systems needs to be evaluated taking into account some possible detrimental aspects. First of all, cost and weight of double wall impingement/effusion scheme are generally higher than simple effusion systems. Moreover, a combination of parameters which maximizes cold side heat transfer may not correspond to an optimal condition in terms of hot side film effectiveness: the ensemble of all the design parameters needs to be considered in order to retrieve the best performance in terms of liner thermal stresses reduction [13]. As a consequence, each particular system requires a dedicated analysis to be performed.

The present work focuses on the measurement of HTC distribution on the cold side of the effusion plate of two distinct impingement/effusion systems with different geometric parameters. The effects of the relative positioning of impingement and effusion arrays, as well as of the impingement jets Reynolds number, are experimentally investigated. The analysis of the heat transfer distribution on the inner side of the effusion plate is supported by CFD simulations: the combination of measured and calculated data enables a complete analysis of thermal and fluid-dynamic phenomena, and thus provides significant information on the unique behaviour of each geometry. A similar approach have been already followed by the authors in the past for the investigation of different cooling configurations based on impinging jets [14, 15, 16].

## 2. EXPERIMENTAL INVESTIGATION

### *2.1. Test rig and measurement techniques*

Measurements were performed in the Heat Transfer and Combustion Laboratory of the Department of Industrial Engineering of the University of Florence (DIEF).

The test rig (depicted in Figure 1) consists of an open-loop, suction type wind tunnel, and is designed to replicate, on an enlarged scale, the thermal and fluid-dynamic phenomena of a combined impingement/effusion cooling system. The vacuum system is composed by four inverter controlled vacuum pumps, with a total maximum capacity of about 2400 $m^3/h$, which pull air at ambient pressure and temperature into the rig inlet section. Since a transient technique is used for heat transfer measurements, air needs to undergo a fast and uniform temperature change. As a consequence, the first component encountered by the air flow is an ad-hoc prepared six stage mesh heater. The number of active stages is defined by the required thermal

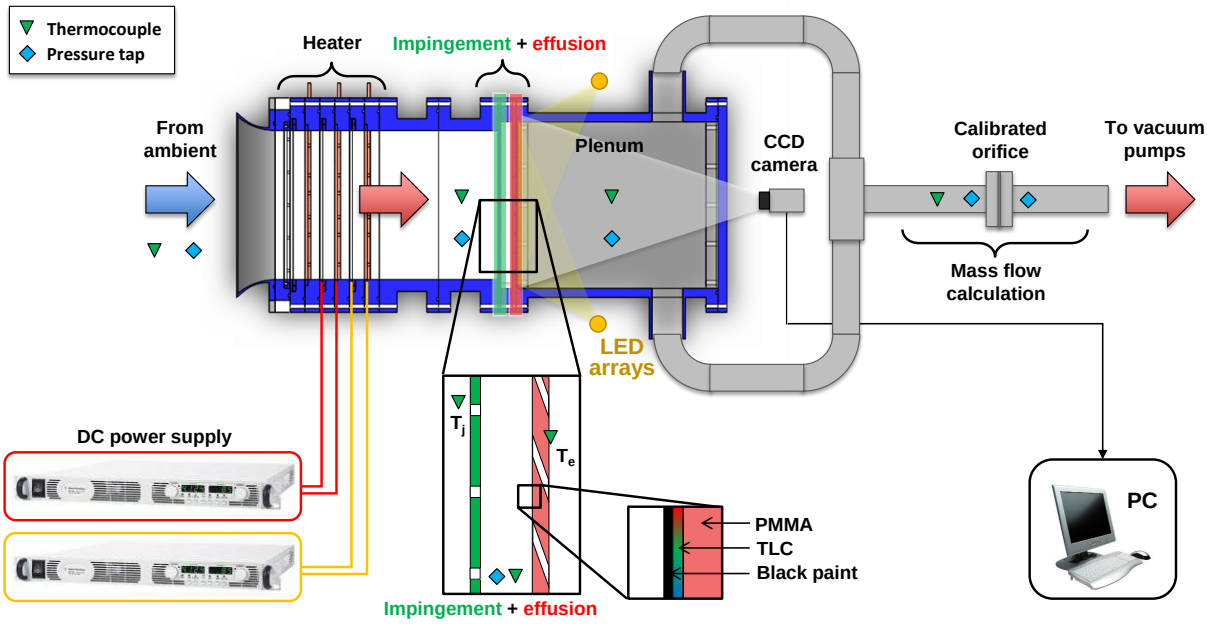


Figure 1: Test rig scheme.

power. Electric power is provided to the stages by dedicated DC power supplies. A straight PMMA duct connects the mesh heater to the cooling geometry model. The small length (200 $mm$) and the low thermal conductivity of the material (0.19 $W/mK$) allow to preserve the uniform temperature profile of the heated air flow.

The cooling geometry is entirely made of transparent PMMA to provide both thermal insulation and optical access to the inner surfaces. The impingement/effusion system is replicated by two parallel plates, housing the impingement (I) and effusion (E) holes arrays, and a spacer, built as a square frame, which separates the two plates and defines the impingement-to-target plate spacing.

Two main configurations have been investigated, which will be referred to as Geometry 1 and 2. The corresponding impingement and effusion plates will be indicated as I1 and E1 for the first Geometry, and I2 and E2 for the second one. A scheme of such geometries is reported in Figure 2. Each configuration presents an equal number of impingement and effusion holes, arranged in staggered arrays. Geometric features of the two geometries are summarized in Table 1, namely impingement jet-to-jet spacings in both orthogonal directions $x$ and $y$ defined on the plate itself ($X$ and $Y$), jet-to-target plate spacing ($Z$), effusion hole diameter ($D_e$), impingement and effusion plates thickness ($S_i$ and $S_e$). All values are scaled with respect to the impingement hole diameter ($D_i$). The inclination of holes axes with respect to the plate surface ($\beta_i$ and $\beta_e$) is also reported, as well as the number of impingement and effusion holes $N_i$ and $N_e$.

Differences in geometric features of the two schemes reflect their design targets. The two geometries share the same values of impingement and effusion plate thickness, as well as the same gap between them. Geometry 1 is designed in case of low coolant availability, thus presenting smaller holes and features aimed at the

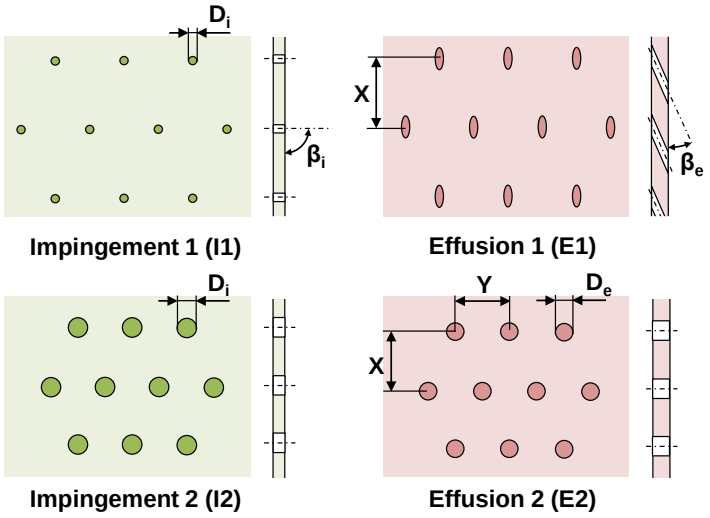


Figure 2: Schemes of Geometry 1 and 2 impingement and effusion plates.

maximization of heat pickup (e.g. inclined effusion holes). On the other hand, Geometry 2 is more suitable when a higher amount of coolant flow is available, and thus houses bigger diameter holes. The analysis of such geometries allows to determine whether variations of corresponding geometric or fluid dynamic features have similar effects for very different systems, which is the main goal of this work.

Heat transfer performance of an impingement/effusion cooling system also depends upon the relative position of the impingement and effusion holes ([8, 10, 17]). To investigate such dependency, two different relative arrangements were examined for both Geometry 1 and 2. In the first arrangement, which will be referred to as Assembly 1 (A1), the projections of the impingement holes on the effusion plate lie midway between the effusion holes in both orthogonal directions (i.e. the two arrays are shifted of $\frac{1}{2}\ X$ in the $x$ direction and $\frac{1}{2}\ Y$ in the $y$ direction). In the second arrangement, which will be named Assembly 2 (A2), the rows of impingement and effusion holes are aligned, but each hole is shifted of $\frac{1}{2}\ Y$ in the $y$ direction. Following this choice of parameters, Assembly 1 presents impingement jets which are almost equally spaced with respect to the three closest effusion holes, while in Assembly 2 impingement jets are midway each set of four effusion hole. Both the assemblies are designed in order to maximize heat transfer on the effusion plate cold side. Figure 3 summarizes the two proposed assemblies, showing the effusion and impingement hole traces on the effusion plate cold side.

Table 1: Investigated systems geometric characteristics.

| **Geometry** | $X/D_i$ [-] | $Y/D_i$ [-] | $Z/D_i$ [-] | $D_e/D_i$ [-] | $S_i/D_i$ [-] | $S_e/D_i$ [-] | $\beta_i$ [°] | $\beta_e$ [°] | $N_i$ [-] | $N_e$ [-] |
|---|---|---|---|---|---|---|---|---|---|---|
| **1** | 10.5 | 10.5 | 6.5 | 1.0 | 1.3 | 2.0 | 90 | 20 | 60 | 60 |
| **2** | 3.0 | 3.0 | 2.5 | 0.90 | 0.5 | 0.7 | 90 | 90 | 54 | 54 |

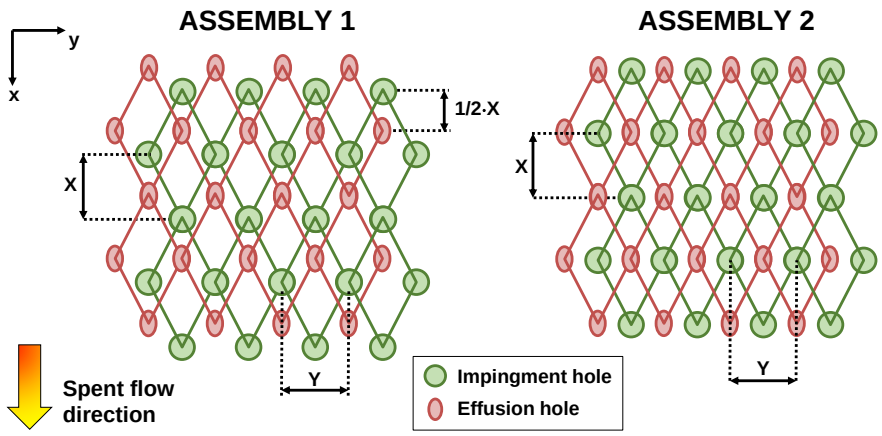


Figure 3: Investigated holes relative positions.

To assess the effect of coolant extraction through the effusion holes, heat transfer has also been investigated for both the impingement arrays paired with a smooth target surface (E0). Coolant extraction is performed by means of two large slots symmetrically located at the opposite sides of the smooth target plate in the $x$ direction, with $30 \times 280\,mm^2$ rectangular cross section. This provides an impingement-only reference case for each geometry where the impingement flow field is only altered by jet-jet interactions and spent coolant flow (crossflow).

A PMMA plenum with an inner volume of $280 \times 280 \times 320 mm^3$ is located downstream of the effusion plate and collects the spent coolant flow, which is then extracted and directed towards the vacuum system.

The aim of this work is to determine heat transfer coefficient distributions on the upstream surface of the effusion plate (effusion cold side). According to the transient HTC measurement approach, the temperature distribution of this surface needs to be monitored during the test. Narrow band thermochromic liquid crystals (TLCs) from LCR Hallcrest with a colour play range between $40°C$ and $41°C$ are used for this measurement. The target heat transfer surface is first sprayed with the TLC coating and then with a water base black paint to provide the TLCs a non-reflecting background. TLCs colour (i.e. surface temperature) evolution is recorded by means of a Sony XCD-SX90CR CCD camera connected to a PC via IEEE 1394b interface. The camera is located outside of the plenum, and observes the heat transfer surface through the effusion plate itself and the rear side of the plenum, which is then designed as a transparent PMMA optical window. Illumination is provided by two 8 W white LED arrays, capable of 750-800 lumen each.

TLCs have been calibrated in the same optical conditions of the actual test, with the aim to obtain an accurate colour-temperature response. To do so, the steady state gradient method [18] has been employed. TLCs and black coating have been applied to a PMMA sheet of the same thickness as the effusion plate. A 4 $mm$ thick, rectangular aluminium plate has then been thermally connected to the TLC coated surface by means of a high conductivity compound. A side of the plate is heated by a cartridge electrical heater, while the opposite side can be cooled down by means of a flow of compressed air. An expanded polyurethane enclosing

thermally insulates the whole assembly from the environment. The plate is designed in such a way that a suitable one-dimensional temperature gradient can be set along its length by regulating the heating power and the air mass flow rate. Nine T type thermocouples (0.5 $K$ measurement accuracy), whose locations are exactly known, measure the plate temperature in as many locations, while a camera records the TLC response: in this way, temperature data can be associated with the TLC colour. To improve accuracy in such a narrow temperature band, thermocouples have been recalibrated using a Pt100 RTD (uncertainty $\pm 0.1K$, level of confidence 95%). The employed measurement technique requires that a specific temperature is associated with a precise event: the most repeatable and evident effect resulted to be the green colour peak intensity, which has then been chosen as the colour descriptor. Calibration has been repeated several times in order to improve the reliability of the results. For the lot of TLCs used for the whole experimental campaign, the calibrations showed a mean value of the green peak at $40.5°C$ with a standard deviation of $0.13°C$.

Local temperature measurements is performed in different points of the rig thanks to several T type thermocouples, connected to a data acquisition/switch unit (Agilent 34970A). This measurement is needed to determine air temperature evolution, requested by transient technique data reduction: a small thermal inertia is thus needed for the sensor to correctly describe air temperature evolution. Air temperature is thus registered by thermocouples with 0.5 $mm$ diameter sheath, directly located upstream the impingement holes: the combination of small sensor volume and high air velocity provides a maximum time constant of around 0.5 $s$ for the thermocouples, which is considered satisfactory for the present case.

Local pressure measurements are performed thanks to a Scanivalve DSA 3217 pressure scanner, housing 16 piezoresistive relative pressure sensors with a maximum accuracy of 6.9 $Pa$. To replicate the desired flow conditions, air mass flow rate is measured on the extraction line through a calibrated orifice, according to the standard EN ISO 5167-1. Mass flow rate is controlled by varying pumps rotating speed.

### *2.2. Test procedure*

As mentioned above, heat transfer tests are performed using a TLC transient technique. The desired flow conditions are initially set by circulating ambient air into the rig, thus keeping the whole geometry at constant ambient temperature. When pressure and mass flow rate reach steady conditions, the camera starts recording (1280×960 resolution at 30 $fps$) and the mesh heater is switched on, thus causing a quick temperature increase of inlet air (around 1.5 $s$ to reach target temperature, which usually ranges from $55°C$ to $65°C$). The test is concluded when the maximum of green intensity in every point of the TLC coated surface is reached.

The transient method for convective heat transfer coefficient $h$ evaluation is based on transient heat transfer between a solid surface and a fluid when the latter undergoes an instantaneous temperature change [19, 20]. Under the hypotheses of one-dimensional conduction and semi-infinite solid, surface temperature evolution

is described by:

$$\frac{T_w(t) - T_{init}}{T_j - T_{init}} = 1 - exp\left(\frac{h^2 \alpha t}{k^2}\right) erfc\left(\frac{h\sqrt{\alpha t}}{k}\right) \quad (1)$$

where $T_w$ is the surface temperature, $T_{init}$ is the initial wall temperature, $T_j$ is the air temperature, $t$ is the time elapsed from air temperature change and $\alpha$ and $k$ are thermal diffusivity and conductivity of the wall material (PMMA in the present case) respectively. Heat transfer distribution can be calculated from equation 1 if the time employed to reach the green peak intensity is known for every point of the TLC coated surface, as well as the temperature corresponding to this peak (thanks to TLC calibration). Since in the present case a quick, yet not instantaneous air temperature step could be realized, the principle of superimposition has been applied to model gas temperature profile in the data reduction procedure, according to the approach firstly introduced by Metzger and Larson [21]. The semi-infinite solid hypothesis has been verified by ensuring that test duration is lower than the limit condition proposed in the study of Vogel and Weigand [22] ($t_{max} < S_e^2/4\alpha$ for the present case).

Flow conditions are identified by the impingement jet Reynolds number, defined as:

$$Re_j = \frac{\dot{m} D_i}{N_i A_i \mu} \quad (2)$$

where $\dot{m}$ is overall air mass flow rate, $A_i$ is the impingement hole cross-section and $\mu$ is air dynamic viscosity. Since target temperature establishes quickly after the beginning of the test and undergoes little variation along the test duration, jet Reynolds number can be considered as constant during the test and thus air dynamic viscosity is calculated at the target temperature itself. Reynolds numbers ranging from around 2500 to 10000 have been investigated for Geometry 1, while Geometry 2 has been tested at a single $Re_j$ value of around 15700. Convective heat transfer coefficient values have been reformulated in a dimensionless form as Nusselt number values, defined as:

$$Nu = \frac{h D_i}{k_j} \quad (3)$$

where $k_j$ is air thermal conductivity, evaluated using the almost constant air temperature after the step change. For every test, the results in terms of Nusselt number distributions will be presented normalized as $Nu/Nu_0$, where $Nu_0$ is the area averaged $Nu$ measured in Row 1 regions (see Figure 6(a)) for the test configuration with Geometry 2 impingement plate (I2) and smooth target surface (E0) at around $Re_j = 15700$. As will be discussed in the validation section this value is in agreement with the averaged Nusselt number (around 7% below) predicted by Bailey and Bunker correlation [23] of Eq. 4. This kind of normalization allows to appreciate the relative difference between the geometries and the relative impact of flow conditions.

### *2.3. Measurement uncertainty*

The uncertainty analysis has been performed according to the standard ANSI/ASME PTC 19.1 [24], based on the Kline and McClintock method [25]. A maximum uncertainty of 2.2% has been determined on $Re_j$, with typical values ranging from 1.5% to 2%. The same approach has been applied to the Nusselt number evaluation. Given the employed technique, the uncertainty on $Nu$ depends upon the accuracy of

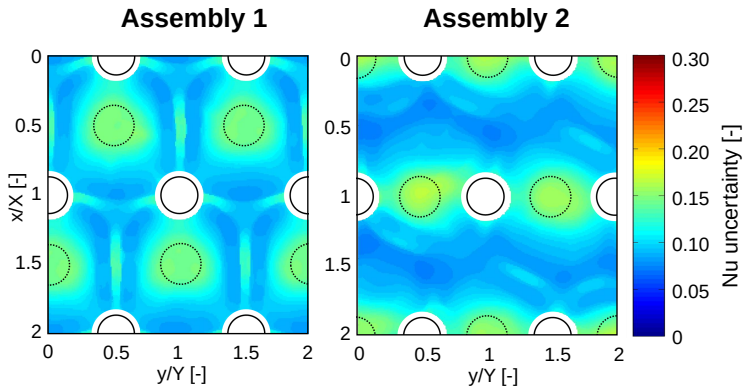


Figure 4: Uncertainty distribution for Geometry 2 at around $Re_j = 15700$.

temperature measurement (both of TLCs and thermocouples) and wall material properties, as well as upon measurement sample rate (given by data acquisition and camera framerate). Figure 4 presents a typical distribution of $Nu$ measurement uncertainty.

For local $Nu$ values, uncertainty can be as high as 20% where heat transfer peaks occur (due to the quick TLC colour play), while values below 10% are present in every other region. Maximum uncertainty on area averaged $Nu$ value is 12% (for Geometry 1, Assembly 1 test at around $Re_j = 7400$), with typical values falling in the range of about 8-10%. All the reported uncertainties bounds are based on a 95% confidence level.

## 3. CFD MODELLING

As a consequence of the employed experimental setup, heat transfer measurement is not possible or at least not reliable in some localized regions, e.g. in the zones covered by the Geometry 1 inclined effusion holes (due to limited optical access) and in the immediate surroundings of effusion holes (due to unreliability of one-dimensional transient heat transfer hypothesis). This issue suggests the opportunity to exploit CFD to have a better insight into the actual heat transfer distribution and flow field. Steady RANS and unsteady SAS calculations were carried out for the four impingement/effusion configurations.

Figure 5 presents a sketch of the computational domain for Geometry 1 (I1E1). Mass flow rate and total temperature were assigned as inlet boundary conditions, whereas a static pressure condition was prescribed at the outlet. The prescribed values are derived from the ones measured during the experiments, chosen in order to match the average jet Reynolds number. All the walls were treated as smooth and adiabatic with a no slip condition, except for the target plate, to which a constant temperature condition was applied. The translational geometrical and fluid dynamic periodicity allows to reduce the computational effort considering only two rows in the streamwise ($x$) direction. A further reduction is achieved imposing a symmetry condition in the spanwise ($y$) direction.

ANSYS Meshing was used to generate the computational grid depicted in Figure 5. A quite coarse sizing was used in the plena, while a mesh refinement was performed in the proximity of the impingement and

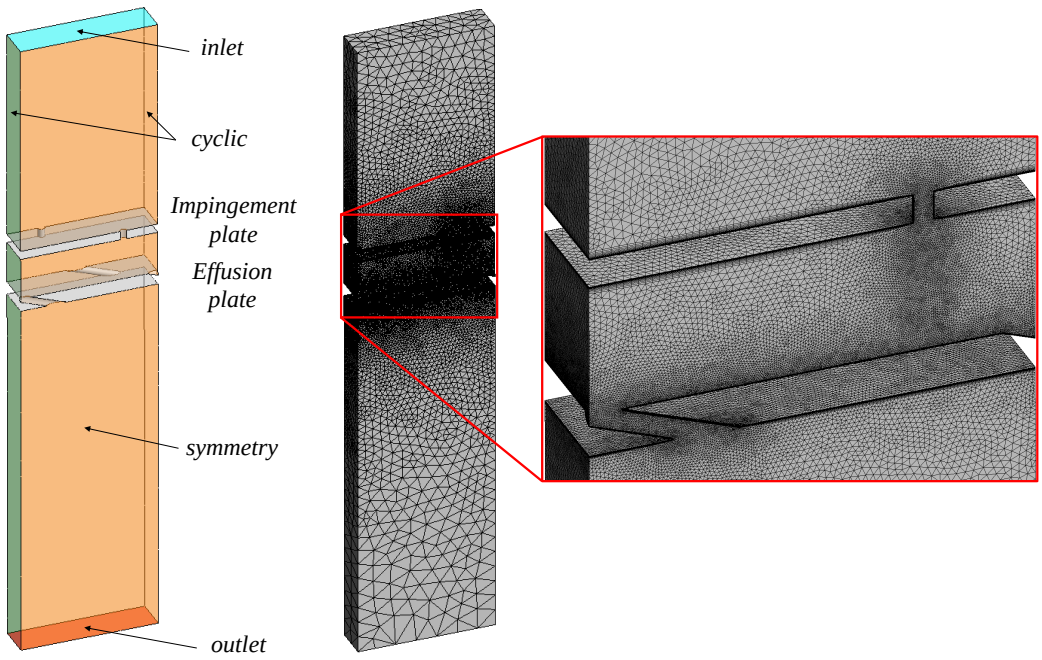


Figure 5: Computational domain and grid.

effusion holes, according to the results of a mesh sensitivity analysis (not reported for the sake of brevity). Approximately, fifteen elements per hole diameter were used to discretize the perforations. The hybrid unstructured mesh is composed of tetrahedrons and a layer of 15 prisms on the target plate, thus retrieving a $y^+$ value around unity. As a result, computational grids with a total of $4.3 - 4.5 \cdot 10^6$ elements and $1.10 - 1.25 \cdot 10^6$ nodes were generated.

Steady RANS calculations were carried out using the Navier-Stokes solver ANSYS Fluent v16.2. The fluid was treated as an ideal gas with variable properties: thermal conductivity, dynamic viscosity and specific heat capacity at constant pressure are considered temperature-dependent. The second order upwind scheme was used to provide an accurate solution. Turbulence was treated using the $k - \omega$ SST turbulence model, which, according to Zuckerman and Lior [26] provides the most accurate results among two-equation eddy viscosity models. The Wall Integration treatment was recovered thanks to the cell clustering on the surfaces of interest.

Geometry 2 Assembly 1 was also investigated using an unsteady CFD approach, since results have shown that this configuration is strongly influenced by flow unsteadiness effects (see section 4.3). In this case, turbulence modelling was treated using Scale Adaptive Simulation (SAS), a hybrid RANS-LES model, in its formulation made available by the solver, based on the $k - \omega$ SST model. In this calculation, the computational domain has the same streamwise extension of the one employed with RANS simulations, but is twice as wide in the spanwise direction, in order to remove the symmetry plane boundary. A whole impingement jet is thus simulated, obtaining a complete solution of the associated unsteady flow structures. This resulted in a computational grid composed of $8.96 \cdot 10^6$ elements. The simulation was carried out with a time step

of $2 \cdot 10^{-5} s$, derived from a sensitivity analysis and resulting to be small enough to provide a convective Courant number lower than 1. Equations were discretised with the Second Order Backward Euler scheme. The simulations were stopped after $6 \cdot 10^{-3} s$, a time frame able to consider at least three passages through the impingement cavity.

## 4. RESULTS

The obtained experimental and numerical results will be presented in the following paragraphs. Given the relevant number of geometries and configurations, all the cases investigated in this work are summarized in Table 2.

Table 2: Summary of the investigated geometries and conditions.

| Impingement | Effusion | Assembly | jet Reynolds number |
|---|---|---|---|
| I1 | E0 | – | 7400 |
| | E1 | A1 | 2500-5000-7400-10000 |
| | | A2 | 2500-5000-7400-10000 |
| I2 | E0 | – | 15700 |
| | E2 | A1 | 15700 |
| | | A2 | 15700 |

### *4.1. Validation*

The results presented in the following paragraphs are obtained from the first experimental campaign performed on the test rig described above: as a consequence, experimental procedure and results need to be validated. This goal is achieved by comparing the results obtained with impingement only configuration with the outcomes of impingement correlations available in the open literature. In particular, Bailey and Bunker [23] correlation is considered, since the configuration obtained combining impingement plate 2 (I2) with the smooth target surface (E0) presents geometric parameters which correspond to its validity ranges. Using the nomenclature employed in this work, the correlation can be expressed as:

$$Nu = 47.1 - 5.5\frac{X}{D_i} + \frac{Z}{D_i}\left(7.3 - 2.3\frac{Z}{D_i}\right) + Re_j\left(4\text{e}{-3} - 1.3\text{e}{-4}\frac{X}{D_i} - 1.5\text{e}{-8}Re_j\right) + \\ + \frac{G_c}{G_j}\left(61.2 - 13.7\frac{X}{D_i} - 28\frac{Z}{D_i}\right) \quad (4)$$

where $G_c$ and $G_j$ represent the ratios of mass flow rate and passage area for impingement cavity and jet respectively. $Nu/Nu_0$ distribution for the test performed at around $Re_j = 15700$ is reported in Figure 6(a) The two extraction slots (located above and below the surface presented in Figure 6(a)) give birth to a symmetric flow field, which can be identified as generated by two equal, undisturbed impingement

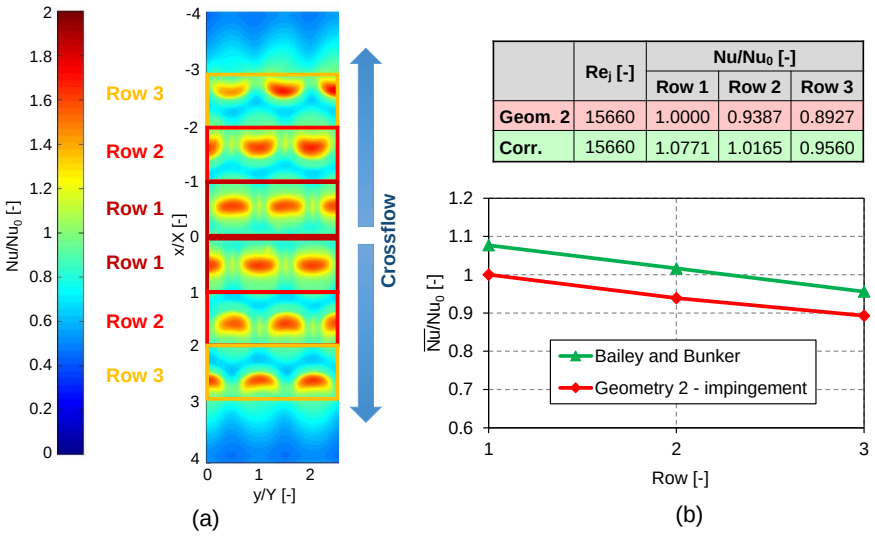


| | $Re_j$ [-] | $Nu/Nu_0$ [-] | | |
|---|---|---|---|---|
| | | Row 1 | Row 2 | Row 3 |
| Geom. 2 | 15660 | 1.0000 | 0.9387 | 0.8927 |
| Corr. | 15660 | 1.0771 | 1.0165 | 0.9560 |

Figure 6: $Nu/Nu_0$ distribution at around $Re_j = 15700$ test (a) and comparison with Bailey and Bunker [23] correlation (b).

arrays. According to that, the row-by-row area averaged $Nu$ values reported in Figure 6(b) are calculated as the average of each couple of symmetric rows. It can be noticed that data from the experiment and the correlation agree both in terms of values and trends, with discrepancies falling below the experimental uncertainty (differences ranging from 7.1% to 8.3%). The experimental procedure and apparatus employed in the present study can thus be considered validated.

### *4.2. Geometry 1*

Figure 7 reports $Nu/Nu_0$ distributions for Geometry 1 for the two hole assemblies obtained at $Re_j = 7400$. Geometry 2 results will be presented separately in the following paragraphs, given the considerable differences between the two configurations. The effusion holes locations (solid lines) and the projections of impingement holes on the investigated surface (dashed lines) are also reported in the maps. White areas hide the regions which are covered by the inclined effusion holes. Moreover, also the regions in which the hypotheses of transient technique (one dimensional conduction and semi-infinite wall) are not verified are excluded from the analysis.

Jet-jet interactions seem to be weak, likely due to the relatively high jet-to-jet distance. The effect of impingement/effusion holes relative positioning can be appreciated by comparing the maps corresponding to the two investigated assemblies, reported in Figure 7. The general shape of heat transfer pattern is similar for the two assemblies. By observing the distributions in closer detail, a slight shift of the peak location towards the positive $x$ direction can be identified for Assembly 2, as well as a less circular shape of the $Nu/Nu_0$ distribution, which seems to be slightly enlarged towards the same positive $x$ direction. If heat transfer magnitude is considered, significantly higher $Nu/Nu_0$ peaks are recorded for Assembly 1, while far from the jet stagnation and around the effusion holes only slight differences can be noticed.

Considering Figure 8, it can be noticed that both the pattern and the magnitude of $Nu$ contours are

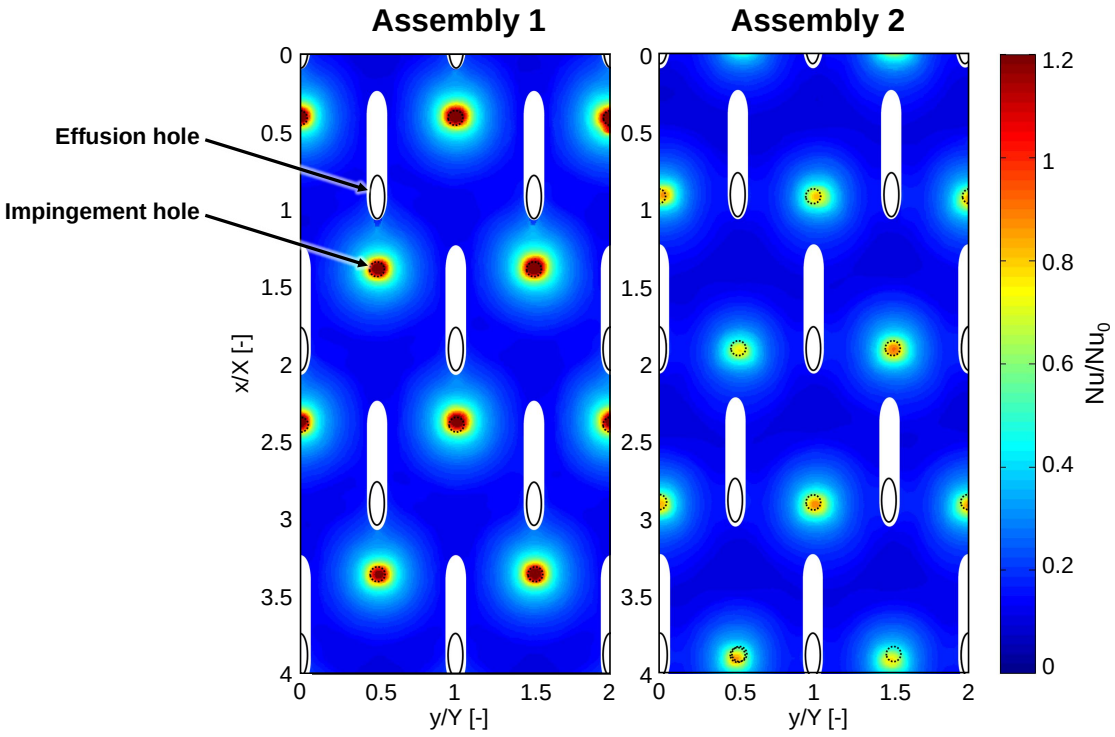


Figure 7: $Nu/Nu_0$ distributions for Geometry 1 (I1E1) at around $Re_j = 7400$.

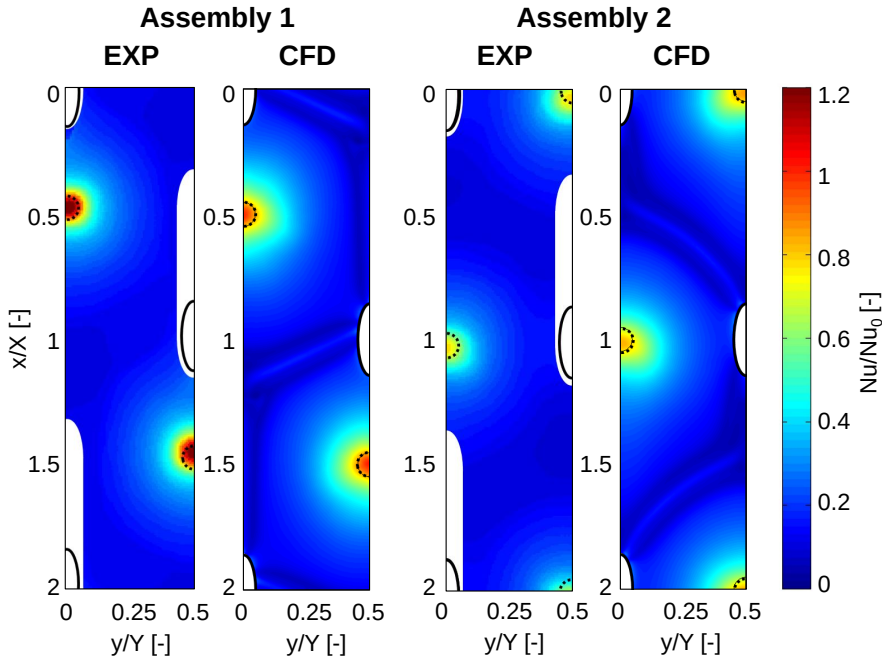


Figure 8: $Nu/Nu_0$ distributions for Geometry 1 (I1E1) at around $Re_j = 7400$: comparison between experimental data and RANS simulations.

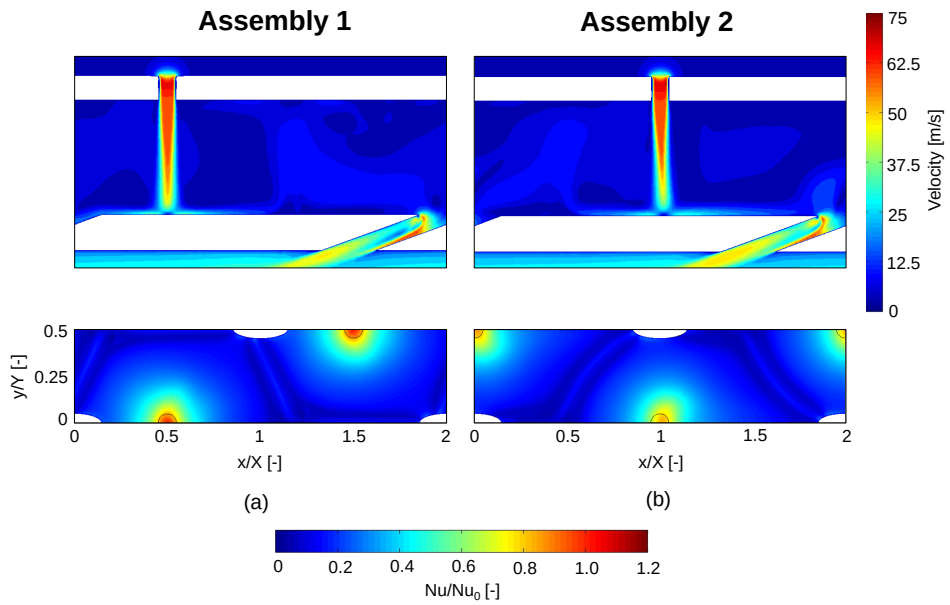


Figure 9: Flow field predicted by CFD for Geometry 1 (I1E1) at around $Re_j = 7400$.

reasonably replicated by the RANS CFD simulations: local discrepancies with experimental data range from 5% to 17% and average discrepancies are approximately 10% (corresponding to an absolute difference $|Nu_{CFD} - Nu_{exp}|$ of around 1.7), which fit within the expected values for the computational model [26] and are very close to the experimental uncertainty. This allows to exploit numerical predictions for obtaining a better understanding of flow physics within the system and its impact on heat transfer characteristics.

The predicted flow field provided by CFD on the left symmetry plane ($y/Y = 0$) is reported in Figure 9. Some interesting discussions can be drawn if this is analysed together with the corresponding heat transfer map. The different $Nu$ peak value of the two assemblies near the jet stagnation region can be interpreted as the effect of the impingement/effusion pattern characteristic of each assembly. For Assembly 1 the impingement jet appears to be approaching the target plate following a straight trajectory, an expected behaviour due to the absence of a dominant crossflow. Nevertheless, when the Assembly 2 is considered, the jet seems to be attracted by the right effusion row, leading the impingement jet to be bent towards the positive $x$ direction. This phenomenon is similar to the typical effect of a crossflow, as confirmed by the kidney-shaped stagnation region (see for example Row 3 in Figure 6), hence justifying the detrimental impact on the cooling performance observed for the Assembly 2 configuration.

#### *4.2.1. Effect of Reynolds number*

The effect of different mass flow rates on impingement/effusion cooling performance has been assessed by performing four tests for each Geometry 1 assembly, so to explore $Re_j$ values ranging from 2500 to 10000. Figure 10 presents the $Nu/Nu_0$ distributions obtained with Assembly 2. The maps show that a variation of $Re_j$ in the investigated range does not significantly influence the shape of $Nu/Nu_0$ pattern, while heat transfer is enhanced by an increase of $Re_j$ in every point of the map. Similar considerations can be derived

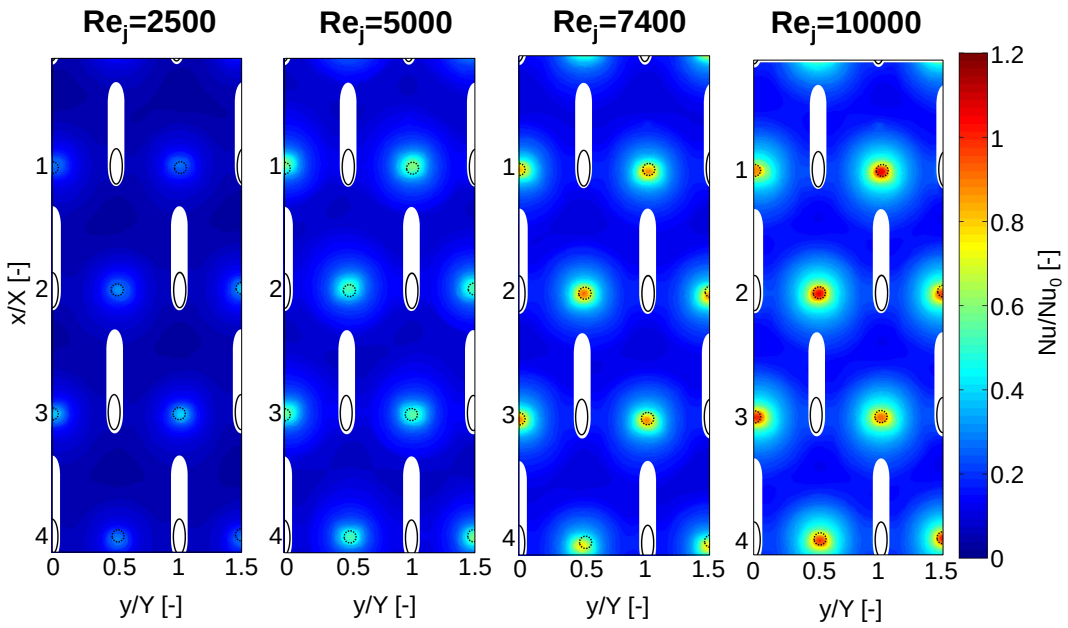


Figure 10: $Nu/Nu_0$ distributions for Geometry 1, Assembly 2 for different $Re_j$ values.

from the Assembly 1 distributions, which are not reported for the sake of brevity.

More comprehensive conclusions can be drawn by comparing area averaged $Nu$ values for the investigated cases. As shown in Figure 11, Assembly 1 outperforms Assembly 2 for the whole $Re_j$ range, which demonstrates that the flow phenomena causing this difference occur in every investigated condition. Even so, the relative differences decrease from 33% to 19% as $Re_j$ increases, and the power law fittings of the two data sets (solid lines) show a slightly stronger heat transfer enhancement of Assembly 2 as $Re_j$ grows. The latter fact seems to indicate that the detrimental effect of locally induced jet deflection verified for Assembly 2 is reduced if impingement jet momentum increases.

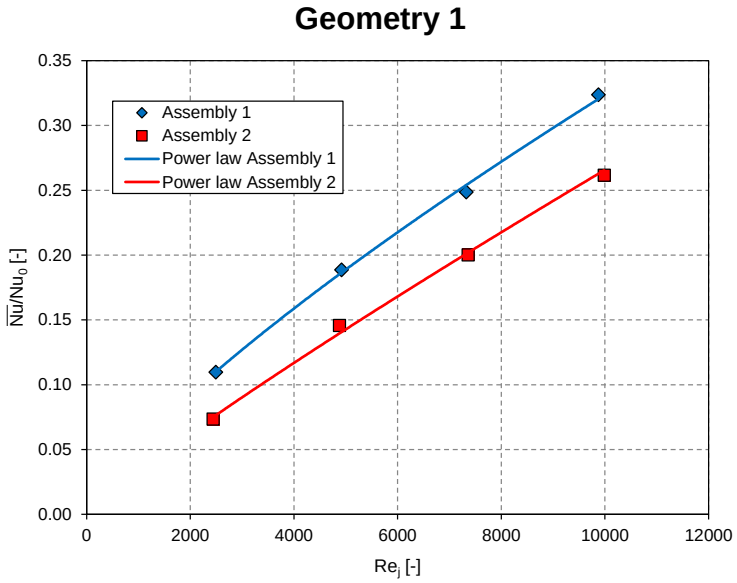


Figure 11: Effect of $Re_j$ on area averaged $Nu$ values for Geometry 1.

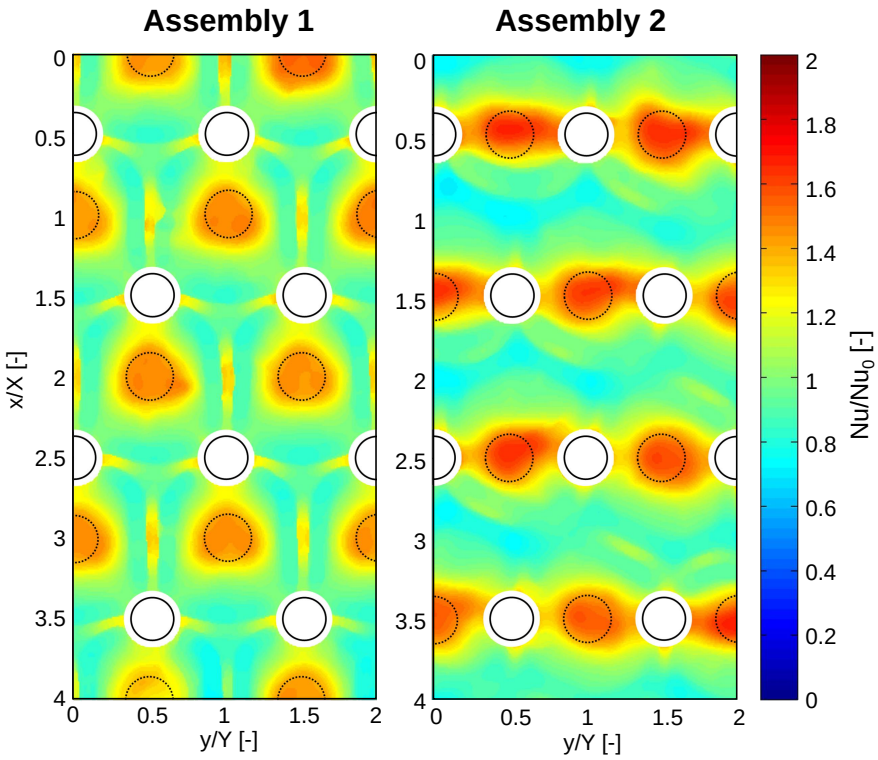


Figure 12: $Nu/Nu_0$ distributions for Geometry 2 (I2E2) at around $Re_j = 15700$.

### *4.3. Geometry 2*

Figure 12 presents $Nu/Nu_0$ distributions obtained for Geometry 2 at around $Re_j = 15700$ for the two investigated assemblies. Effusion holes locations and impingement holes projections are reported with the same notation of Figure 7.

For this geometry, the presence and location of effusion holes strongly influence the spatial distribution of heat transfer. For Assembly 1 a heat transfer peak is located below each impingement hole, as recorded for Geometry 1: in this case, however, a rather complex pattern of this region is observed, with three distinct lobes directed towards the nearest effusion holes. This behaviour also extends to the surroundings of the stagnation region. Secondary high heat transfer regions are present between adjacent jets, elongated in shape and perpendicular to a line linking the jet impact locations. The cause of these secondary peaks can be identified in the fountain effect, already observed and described by Cho and Rhee [5]. According to the scheme of Figure 13, two primary vortices arise in the region between two impingement jets, and a low heat transfer region is generated where they detach from the wall. In between the detachment locations two secondary vortices are formed, whose recirculation creates a local impingement effect and thus an increase in heat transfer. A heat transfer peak under each impingement jet is also present for Assembly 2, but its magnitude is significantly higher than the ones recorded for Assembly 1. The peak shape is also deeply different, being elongated in the direction of the two nearest effusion holes. At the same time, low heat transfer zones are present in the areas between the effusion holes rows ($x/X \simeq 1, 2, 3$). This can be ascribed to weak and unstable jet-jet interactions occurring in these areas. For Assembly 2 map, $Nu$ peaks related to

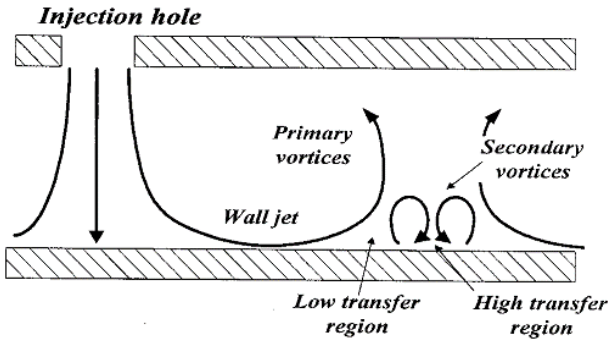


Figure 13: Sketch of the fountain effect (Cho and Rhee [5])

fountain effect are located close to the lower side of the jets in the left part of the distribution ($x/X < 1-1.5$) and close to the upper side on the right part ($x/X > 1-1.5$). Multiple repetitions of the test show that these regions randomly migrate close to the higher or lower side of the jets. These observations can be justified considering the impingement/effusion pattern features. In this case, the low distance between impingement and effusion holes results in a strong interaction between jets and coolant extractions, while far from the rows the lack of confinement induces the generation of flow unsteadiness. This phenomenon is inhibited for Assembly 1, where the coolant bleeding provided by effusion holes tends to stabilize this region, increasing at the same time the heat transfer. Overall, this effect compensates for the reduction of the stagnation region peak value, resulting in an average $Nu/Nu_0$ of 1.07 for Assembly 1 and 1.08 for Assembly 2. Roughly the same heat transfer entity is thus measured for the two configurations, but with a more homogeneous distribution for Assembly 1. This conclusion is coherent with literature results (Cho and Rhee, [5]).

Also CFD simulations performed for Geometry 2 show a reasonable agreement with experimental data, correctly reproducing the heat transfer pattern in the stagnation region (Figure 14). In the areas of jet-jet interactions, i.e. where the fountain effect occurs, the correct behaviour is still replicated, even though CFD solution shows higher gradients with respect to the measured ones. This discrepancy can be interpreted by considering that steady RANS approach returns a frozen solution of a highly unstable aero-thermal field, while in the experimental outcomes only the time averaged result of such unsteadiness is recorded, leading to a smoother measured heat transfer pattern. This fact is particularly evident for Assembly 2, where steady RANS solution omits the time evolution of the unsteady and randomly migrating jet-jet interaction regions and provides instead an ideal, instantaneous $Nu$ pattern. Even so, quantitative agreement is reasonable in both cases, with discrepancies on area averaged heat transfer falling below $\pm 5\%$ ($+2.5\%$ for Assembly 1, corresponding to a difference $Nu_{CFD} - Nu_{exp} = 2.2$, and $-4.5\%$ for Assembly 2, corresponding to a difference $Nu_{CFD} - Nu_{exp} = -4.0$). The predicted flow fields shown in Figure 15 clearly highlights a similarity with the sketch in Figure 13, with the formation of the primary and secondary vortices typical of fountain effect. As expected, a much better agreement is present between the results of the experiment and of the scale resolving SAS simulation. In Figure 16 the experimental $Nu/Nu_0$ distribution on the effusion plate cold side

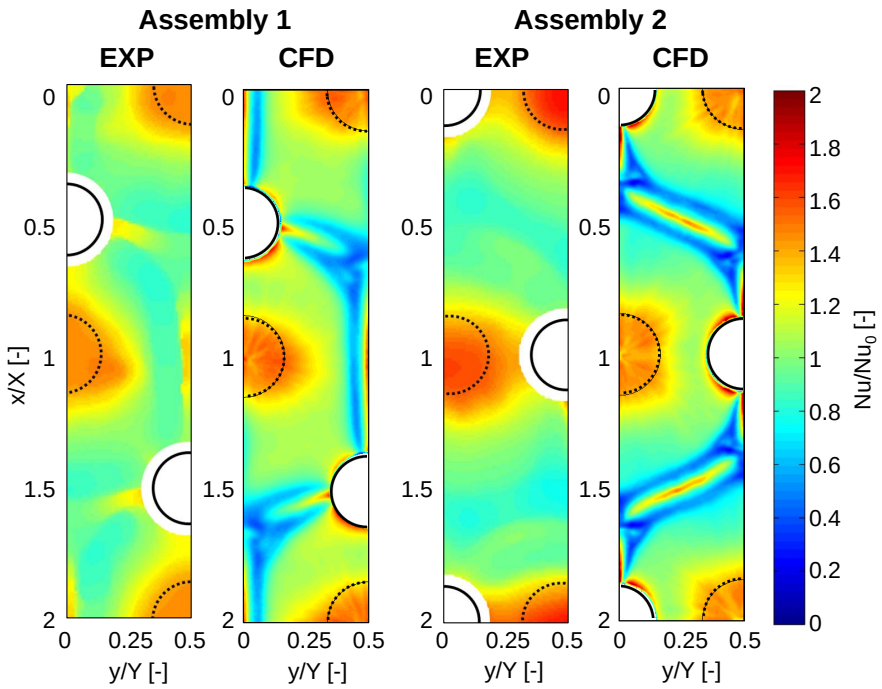


Figure 14: $Nu/Nu_0$ distributions for Geometry 2 (I2E2) at around $Re_j = 15700$: comparison between experimental data and RANS simulations.

is compared with the time averaged one obtained from the simulation. Slightly higher heat transfer gradients and a small overestimation of the peaks are still present in the computed distribution, but the pattern shape and entity are replicated in a more accurate way with respect to the steady RANS simulation. In fact, the scale resolving simulation allows to determine the role of unsteadiness in defining the heat transfer pattern:

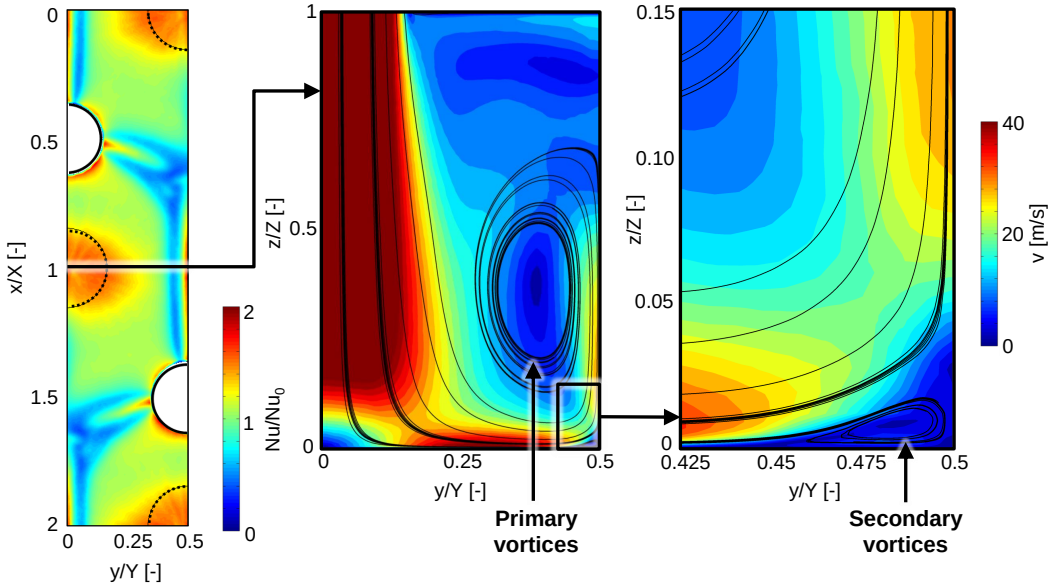


Figure 15: Flow field predicted by CFD for Geometry 2 Assembly 1 (I2E2-A1) on the $x/X = 1$ plane at around $Re_j = 15700$.

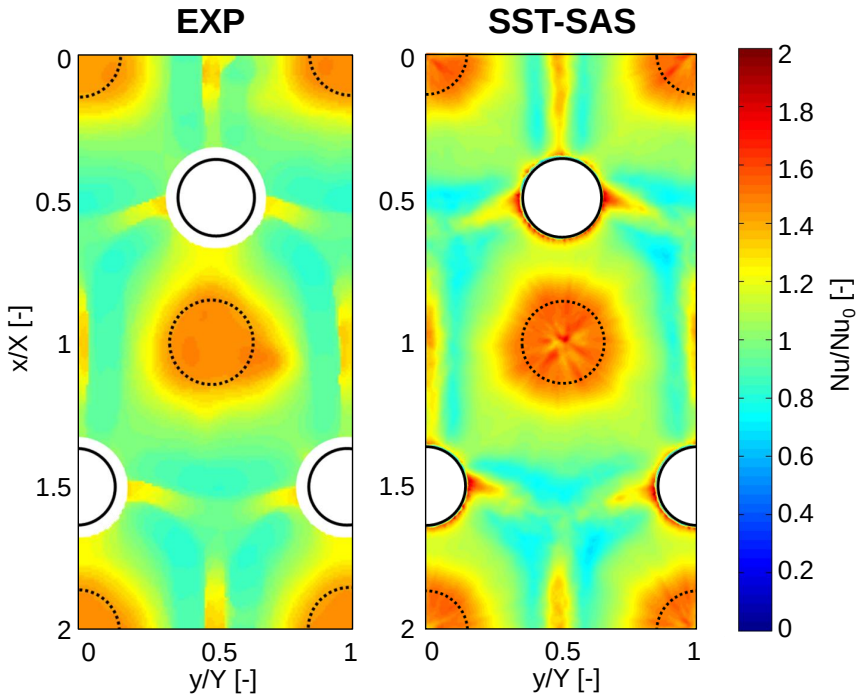


Figure 16: $Nu/Nu_0$ distributions for Geometry 2 Assembly 1 (I2E2-A1) at around $Re_j = 15700$: comparison between experimental data and SAS simulation.

as shown in Figure 17, the instantaneous heat transfer distribution is strongly different from the average pattern, which is the one provided by the experiments. This is due to the large scale shear layer vortices (also visible in Figure 17), which get transported by the jet, impact onto the target surface, travel along the

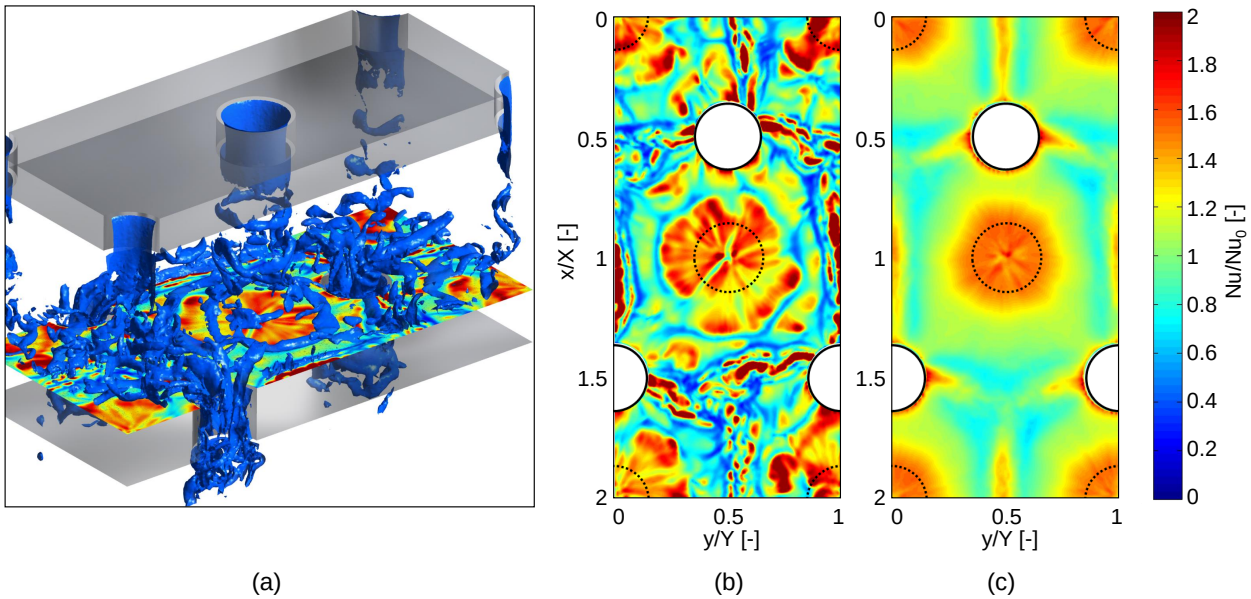


Figure 17: Effect of flow unsteadiness on heat transfer for Geometry 2 Assembly 1 (I2E2-A1) at around $Re_j = 15700$: vorticity structures (a) and corresponding instantaneous $Nu/Nu_0$ distribution (b) compared with the time averaged one (c).

wall jet region and then interact with the corresponding structures coming from the surrounding jets. Strong local differences in heat transfer are generated by a similar flow field, which move along the surface together with the corresponding flow structures. In this case, the computed area averaged $Nu$ value is around +9.6% higher then the experimental one, which is a higher value than the one recorded for the RANS simulations: this is due to the fact that the strong underestimation of low heat transfer regions of the RANS compensated the overestimation of heat transfer peaks in average terms. This does not happen for the SAS simulation, where the low heat transfer zones are correctly replicated and thus the recorded discrepancy only reflects the slight overestimation of the peak regions. In any case, it should be noticed that all of these discrepancies are comparable with the evaluated experimental uncertainty.

### *4.4. Effect of coolant extraction*

Impingement 1 and 2 geometries (I1 and I2) have also been tested with a smooth target surface (E0), with the aim to study the effect of coolant extraction on impingement heat transfer. Figure 18 and Figure 19 show the outcomes of such investigation, together with the corresponding heat transfer distributions obtained with effusion holes. The maps show that significantly different effects of coolant extraction are present for the two geometries. For Impingement 1 (Figure 18) effusion holes seem not to dramatically alter the heat transfer pattern shape. However, if the distributions are observed in closer detail, particular similarities can be identified for the first row ($0 < x/X < 1$) between I1E0 and I1E1-A1 configurations, since the peak region appears to be almost circular in shape and the peak is located directly under the impingement hole in both cases. For the I1E0 configuration the first row can be considered unaffected by the spent coolant flow (crossflow), which is directed towards the positive $x$ direction: this fact confirms that effusion holes in Assembly 1 configuration do not significantly deflect the impingement jet. As a consequence, the main effect of coolant extraction consists in the higher peak $Nu/Nu_0$ values: this can be due to a stabilizing effect of coolant extraction on the jet itself, which reduces spent coolant flow recirculation (Hollworth et al. [8]) and interaction with the free jet region and thus minimizes jet momentum losses, which in this case can play a significant role given the relevant jet-to-target plate spacing ($Z/D_i = 6.5$).

A similar heat transfer pattern is also present for the third row ($2 < x/X < 3$) between I1E0 and I1E1-A2 configurations: in both cases, a slightly kidney-shaped $Nu/Nu_0$ distribution is present near the jet impact location, and peak values are also similar. For I1E0 configuration the crossflow generated by the first two rows of impingement holes runs over the third one, deflecting the jets and decreasing heat transfer (Bailey and Bunker [23]). In the present case, the effect is slight due to the considerable jet-to-jet distances and height of impingement cavity. This fact however confirms the hypothesis, already highlighted by CFD results, that the lower values of Assembly 2 with respect to Assembly 1 are due to a phenomenon similar to a local crossflow, due to the effusion holes themselves.

For Impingement 2 (Figure 19), the effect of effusion holes on $Nu/Nu_0$ distribution shape is significant. Without effusion holes (I2E0), $Nu/Nu_0$ peaks elongated in the $y$ direction are recorded, as well as secondary

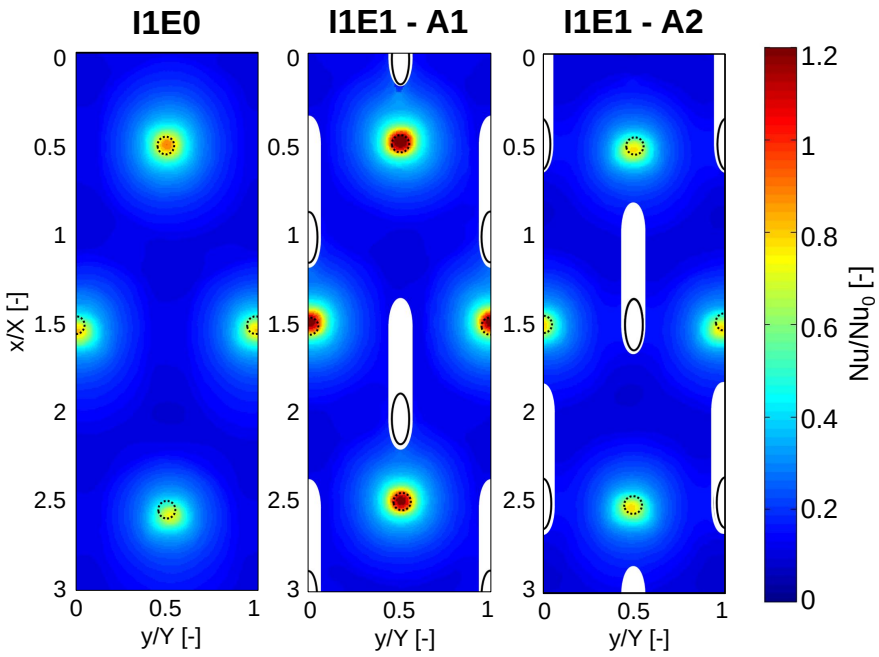


Figure 18: $Nu/Nu_0$ maps for Impingement 1 geometry (I1) at around $Re_j = 7400$.

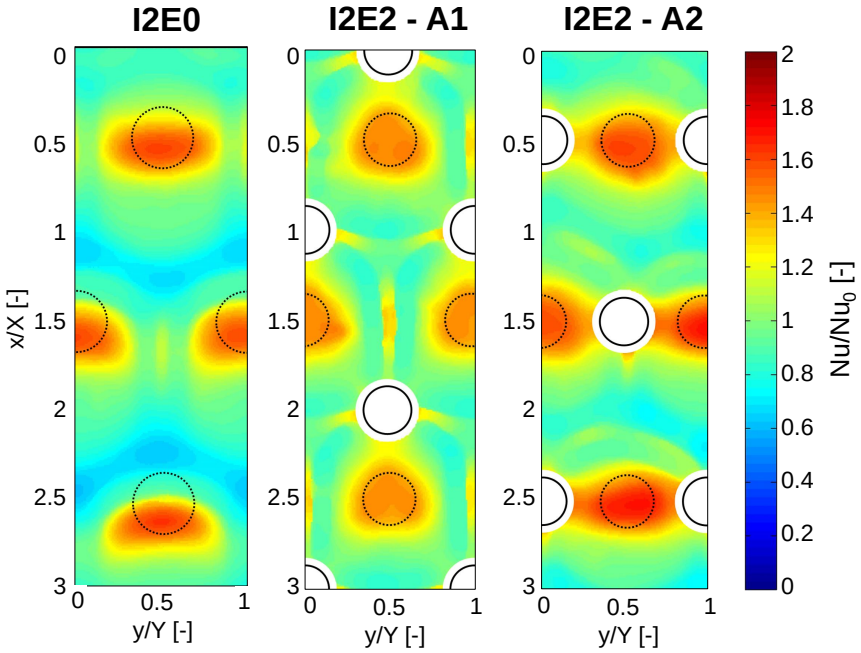


Figure 19: $Nu/Nu_0$ maps for Impingement 2 geometry (I2) at around $Re_j = 15700$.

peaks related to the fountain effect in between adjacent holes of the same row (i.e. at the same $x/X$ values). Given the low $X/D_i$, $Y/D_i$ and $Z/D_i$, crossflow is expected to be significant, and its main effects can be identified in the shape and the shift of the second and third rows peaks and in the clear decrease in peak $Nu/Nu_0$ values. The absence of secondary peaks in between different impingement rows (i.e. with different

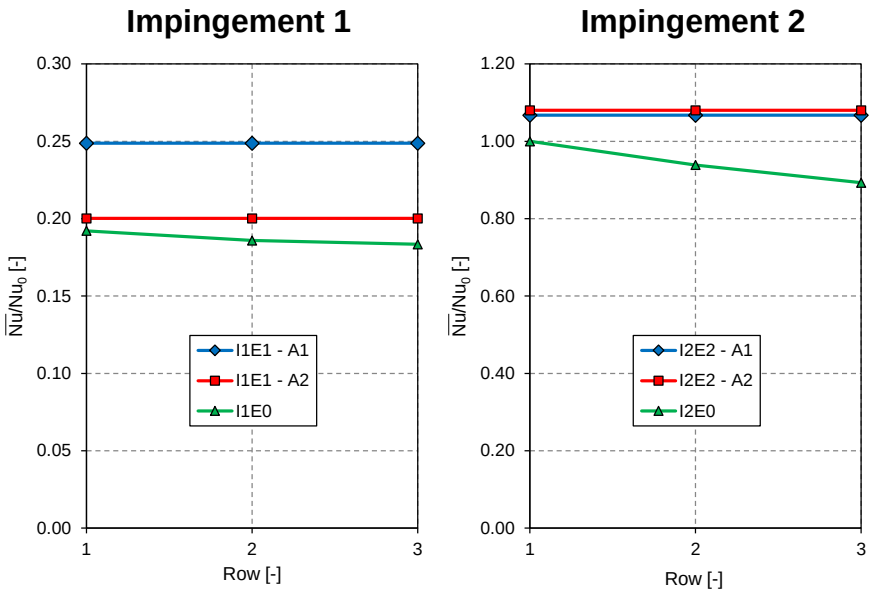


Figure 20: Area averaged $Nu/Nu_0$ values for Impingement 1 and 2 with different target plates and assemblies.

$x/X$ values) could also be interpreted as an effect of the crossflow. If coolant extraction is considered, the positive effect of effusion holes can be observed, causing an increase in secondary peak magnitude and thus in heat transfer uniformity (I2E2-A1) or directly enhancing primary peaks (I2E2-A2).

Further discussions can be drawn out if area averaged $Nu/Nu_0$ values for the cases presented in Figure 18 and Figure 19 are considered (Figure 20): for the cases without effusion, Row 1 values are averaged over the area defined by $0 < x/X < 1$, Row 2 over $1 < x/X < 2$ and Row 3 over $2 < x/X < 3$, while for the sake of clarity area averaged values over the whole surface are reported for the cases with effusion (i.e. constant values of $Nu$ changing the Row number).

For Impingement 1, the slight decrease of E0 values from Row 1 to Row 3 is due to the crossflow: with respect to this baseline case, I1E1-A1 presents area averaged values increases ranging from 29.4% (for Row 1) to 35.6% (for Row 3), while I1E1-A2 presents augmentations ranging from 4.2% (for Row 1) to 9.1% (for Row 3). A clear positive effect of coolant extraction is thus recorded for A1 configuration, while comparable values are present for A2. It must be noticed that the effusion holes traces limit the optical access on the measurements surface and hence the area averaged values for the cases with effusion holes are not evaluated on the whole target surface. However, CFD results allowed to verify that area averaged values decrease of around 7% in the worst case as the effect of such approximation, thus the considerations reported above are still valid.

The results obtained with I2 plate present a stronger crossflow effect with respect to I1 for the impingement only configuration (I2E0), since average heat transfer values strongly decrease passing from Row 1 to Row 3. Values are very similar for the two configurations with effusion holes (I2E2-A1 and A2), as already highlighted before. Considering Row 1, only a slight increase in heat transfer is present with effusion holes (below 8%),

while stronger increases are recorded for Rows 2 and 3 (up to 21%). This leads to the conclusion that the positive effect of effusion holes for Impingement 2 is mainly bound to the suppression of crossflow.

## 5. CONCLUSIONS

In this study, two different impingement/effusion cooling systems have been analysed, with the aim to evaluate heat transfer performance on the effusion wall cold side. The geometries present equal numbers of impingement and effusion holes, both arranged in staggered configurations, but with sparser (Geometry 1) and denser (Geometry 2) arrays. The effect of two different impingement and effusion holes relative positioning is investigated (Assembly 1 and 2), as well as of Reynolds number and coolant extraction.

For the sparser geometry, results present strong primary heat transfer peaks and small jet-jet interactions. For this configuration, the presence of effusion holes causes area averaged $Nu$ to increase up to 30% with respect to impingement only case, without significant differences in heat transfer pattern shape. This has been interpreted as the effect of a reduction of spent coolant flow recirculation. A significant effect of holes assembly is also present: by shifting the hole arrays of $\frac{1}{2}$ holes pitch (i.e. changing the assembly), reductions up to 33% in area averaged $Nu$ are recorded (at around $Re_j = 2500$), since impingement jets are deflected by the effusion holes flow field. The differences between the two assemblies tend to decrease as $Re_j$ increases.

For Geometry 2, heat transfer is strongly influenced by the presence and assembly of extraction holes. Assembly 1 presents a characteristic heat transfer pattern, with clover-shaped primary peaks under the impingement holes and strong secondary peaks midway between the jets induced by the fountain effect. Assembly 2 shows primary peaks elongated towards the two nearest effusion holes and with a higher magnitude with respect to Assembly 1, but also large regions of low and unstable heat transfer: this results in an area averaged $Nu$ values similar to the ones of Assembly 1, but also in a less homogeneous distribution. For both assemblies, significant heat transfer increases are recorded (around 15%) with respect to impingement only configuration, due to the suppression of the intense crossflow generated by the dense hole array.

The results of this study have shown that different geometries provide characteristic results: slight modifications to the cooling system can significantly alter both shape and magnitude of heat transfer pattern, due to the wide range of parameters on which heat transfer depends and the strong interactions between different phenomena. Despite the small number of investigated geometries, some overall considerations can be derived for impingement/effusion systems design:

- For sparse geometries ($X/D_i$ around 10, as Geometry 1) care should be taken so that the internal pressure field does not deflect the jets, thus maximizing heat transfer.

- For dense geometries ($X/D_i$ around 3, as Geometry 2) overall cooling performances show low sensibility to the impingement/effusion holes relative position (at least in the investigated configurations): as a consequence, effort should be made to avoid the occurrence of low heat transfer regions, which can be obtained by making jets impinge in the region farthest from the effusion holes.

- CFD is a suitable tool for predicting fluid and thermal phenomena involved by an impingement/effusion system: steady RANS simulations provide reliable area averaged heat transfer values in the range of $\pm 10\%$, but only unsteady simulations are able to retrieve the correct shape and entity of time averaged Nusselt number distribution.


## Acknowledgement

The research presented in this paper was sponsored by GE-Avio S.R.L. located in Turin, Italy, whose financial contribution is gratefully acknowledged.


## References


[1] A. Andreini, A. Ceccherini, B. Facchini, F. Turrini, I. Vitale, Assessment of a Set of Numerical Tools for the Design of Aero-EnginesCombustors: Study of a Tubular Test Rig, ASME Conference Proceedings (GT2009-48838) (2009) 421–433.

[2] A. Andreini, B. Facchini, L. Mazzei, L. Bellocci, F. Turrini, Assessment Of Aero-thermal Design Methodology For Effusion Cooled Lean Burn Annular Combustors, ASME Conference Proceedings (GT2014-26764).

[3] L. Andrei, A. Andreini, B. Facchini, L. Winchler, A decoupled CHT procedure: Application and validation on a gas turbine vane with different cooling configurations, Energy Procedia 45 (2014) 1087–1096.

[4] H. Cho, R. Goldstein, Effect of hole arrangements on impingement/effusion cooling, in: Proceedings of the 3rd KSME-JSME Thermal Engineering Conference, 71–76, 1996.

[5] H. H. Cho, D. H. Rhee, Local heat/mass transfer measurement on the effusion plate in impingment/effusion cooling system, J. Turbomach. (3) (2000) 601–608, doi:10.1115/1.1344904.

[6] D. H. Rhee, J. H. Choi, H. H. Cho, Flow and heat (mass) transfer characteristics in an impingement/effusion cooling system with crossflow, J. Turbomach. 125 (1) (2003) 74–82.

[7] P. Singh, S. V. Ekkad, Effects of spent air removal scheme on internal-side heat transfer in an impingement-effusion system at low jet-to-target plate spacing, International Journal of Heat and Mass Transfer 108 (2017) 998–1010.

[8] B. Hollworth, G. Lehmann, J. Rosiczkowski, Arrays of impinging jets with spent fluid removal through vent holes on the target surface, part 2: local heat transfer, Journal of Engineering for Power 105 (2) (1983) 393–402.

[9] D.-H. Rhee, P.-H. Yoon, H. H. Cho, Local heat/mass transfer and flow characteristics of array impinging jets with effusion holes ejecting spent air, International Journal of Heat and Mass Transfer 46 (6) (2003) 1049 – 1061, ISSN 0017-9310.

[10] B. Hollworth, L. Dagan, Arrays of impinging jets with spent fluid removal through vent holes on the target surfacePart 1: Average heat transfer, Journal of Engineering for Power 102 (4) (1980) 994–999.

[11] P. Ligrani, Z. Ren, F. Liberatore, R. Patel, R. Srinivasan, Y.-H. Ho, Double Wall Cooling of a Full-Coverage Effusion Plate, Including Internal Impingement Array Cooling, J. Eng. Gas Turbines Power 140 (5) (2018) 051901.

[12] G. Meyers, J. Van der Geest, J. Sanborn, F. Davis, Comparison of advanced cooling concepts using color thermography, in: AIAA 3rd Applied Aerodynamics Conf. AIAA Paper AIAA-85, vol. 1289, 1985.

[13] K. M. Kim, H. Moon, J. S. Park, H. H. Cho, Optimal design of impinging jets in an impingement/effusion cooling system, Energy 66 (2014) 839–848.

[14] B. Facchini, M. Surace, Impingement cooling for modern combustors: Experimental analysis of heat transfer and effectiveness, Experiments in Fluids 40 (4) (2006) 601–611.

[15] A. Andreini, R. Da Soghe, B. Facchini, F. Maiuolo, L. Tarchi, D. Coutandin, Experimental and numerical analysis of multiple impingement jet arrays for an active clearance control system, J. Turbomach. 135 (3).

[16] E. Burberi, D. Massini, L. Cocchi, L. Mazzei, A. Andreini, B. Facchini, Effect of rotation on a gas turbine blade internal cooling system: Numerical investigation, J. Turbomach. 139 (3).

[17] H. H. Cho, D. H. Rhee, R. Goldstein, Effects of hole arrangements on local heat/mass transfer for impingement/effusion cooling with small hole spacing, J. Turbomach. 130 (4) (2008) 041003.

[18] T. L. Chan, S. Ashforth-Frost, K. Jambunathan, Calibrating for viewing angle effect during heat transfer measurements on a curved surface, International Journal of Heat and Mass Transfer 44 (2001) 2209–2223.

[19] P. T. Ireland, Z. Wang, T. V. Jones, Liquid Crystal Heat Transfer Measurements, in: Measurements Techniques, Lecture Series 1993-05, von Karman Institute for Fluid Dynamics, 1993.

[20] C. Camci, Liquid Crystal Thermography, in: Temperature Measurements, Lecture Series 1996-07, von Karman Institute for Fluid Dynamics, 1995.

[21] D. Metzger, D. Larson, Use of melting point surface coatings for local convection heat transfer measurements in rectangular channel flows with 90-deg turns, Journal of Heat Transfer 108 (1) (1986) 48–54.

[22] G. Vogel, B. Weigand, A new evaluation method for transient liquid crystal experiments, in: National Heat Transfer Conf. NHTC2001-20250, California, 2001.

[23] J. Bailey, R. Bunker, Local heat transfer and flow distributions for impinging jet arrays of dense and sparse extent, in: ASME Turbo Expo 2002: Power for Land, Sea, and Air, GT2002-30473, American Society of Mechanical Engineers, 855–864, doi:10.1115/GT2002-30473, 2002.

[24] ASME, Measurement Uncertainty, in: Instrument and Apparatus, vol. ANSI/ASME PTC 19.1-1985 of *Performance Test Code*, ASME, 1985.

[25] S. J. Kline, F. A. McClintock, Describing Uncertainties in Single Sample Experiments, Mechanical Engineering 75 (1953) 3–8.

[26] N. Zuckerman, N. Lior, Jet impingement heat transfer: physics, correlations, and numerical modeling, Advances in heat transfer 39 (2006) 565–631.